Full-Scale Burning Behavior of Combustible Solids—The Impact of Material Composition on Fire Growth, Flame Structure and Heat Feedback

Isaac T. Leventon*, Michael V. Heck, Kevin B. McGrattan, Matthew F. Bundy, Rick D. Davis

100 Bureau Drive; Gaithersburg, MD 20878; United States of America

E-mail: isaac.leventon@nist.gov

Abstract. This paper provides an overview of selected measurements from a series of 90 full-scale fire experiments quantifying the impact of material composition on full-scale burning and fire growth behavior. Samples were selected to provide a wide range of material compositions (i.e., chemistries) and burning behaviors: physical deformation (e.g., swelling, charring collapse, dripping, and/or melt flow), heavy or light soot formation, and varied ignitability and fire growth rates. In total, 18 unique combustible solids were tested including: natural and synthetic polymers, copolymers, fiberglass-reinforced composite materials, porous polymer foams, and electrical cables. Collectively, these experiments offer a comprehensive set of validation data for computational fluid dynamics (CFD) simulations of large scale fire growth due to flame spread over the surface of combustible solids. Here, a subset of these measurements is highlighted: flame heat flux, structure, and heat transfer mechanism.

1. Introduction

The fire modeling community is working to quantitatively predict the ignition, burning rate, and growth of fires spreading over real materials. To address the needs of state-of-the-art fire models, NIST has been developing [1] experimental datasets [2] and analytical tools [3, 4, 5] to determine material thermophysical properties and validate their ability to predict flammability response across a range of configurations. In addition, a comprehensive, searchable, version-controlled data repository has been developed called the NIST Material Flammability Database. This database of experimental measurements, analysis tools, and material property sets is designed to support ongoing development of the Fire Dynamics Simulator (FDS) [6].

This research effort builds upon existing experimental and computational modeling research. Recent advancements in material property determination have been substantial [7], with: (1) varied approaches regarding calibration data sets [8] and optimization targets/techniques [9, 10, 12, 11, 13, 14]; (2) large, and more easily accessible data sets/repositories of milligram- and gram-scale measurements [15, 16, 17]; and (3) promising results simulating the coupled solid- and gas-phase phenomena that control fire behavior at bench, intermediate, and full-scale as well as analysis demonstrating the impact of model calibration approaches, property set values, and/or sub-model choices on final model predictions [18, 19, 20, 21, 22].

The NIST Material Flammability Database contains experimental measurements for model calibration; automated analysis tools for material property calibration; archived, version-

controlled material property sets; and unique datasets to validate model predictions of fire behavior at multiple scales [23]. This database incorporates new measurement data from ongoing and planned future research efforts in the NIST Fire Research Division. Here, we present a summary of selected measurements from a recent series of full-scale flame spread experiments.

2. Experimental Description

A multi-year experimental campaign was conducted to assess the impact of material composition on the full-scale burning behavior of combustible solids [23]. The experimental apparatus used in this campaign is based on an assembly originally developed at FM Global for experiments measuring flame spread rate over combustible wall lining materials [24] (since standardized as FM 4910 [25]). Here, combustible solids approximately 6 mm to 50 mm thick are insulated at their back surface, mounted onto two inert parallel walls each 2.44 m tall by 0.61 m wide, and ignited at their base using a rectangular propane burner (nominal HRR, 60 kW). Figure 1 provides a drawing of the apparatus; details of sample mounting and apparatus construction are provided elsewhere [23]. The characterization of the spatial and temporal variability of the burner and its impact on measured ignitability and fire growth behavior are not reported in detail here; however, average steady state burner flame heat feedback across the base of the panel walls is plotted in Fig. 2 and further analysis is presented elsewhere [23].

The following measurements were recorded in these full-scale experiments:

- Initial and final sample mass
- Time-resolved measurements of fire size (i.e., heat release rate, HRR), soot generation, and gaseous species production (CO and CO_2)
- Ignition time, average fire growth rate, peak HRR, and total heat released (in response to a well-characterized ignition source)
- Temporally and spatially-resolved measurements of flame heat flux and heat transfer mechanism (total and radiative) [these measurements are highlighted in this paper]
- Radiative heat flux at a distance
- Heat of combustion and species yields (Y_{CO}, Y_{CO_2} and Y_{soot})

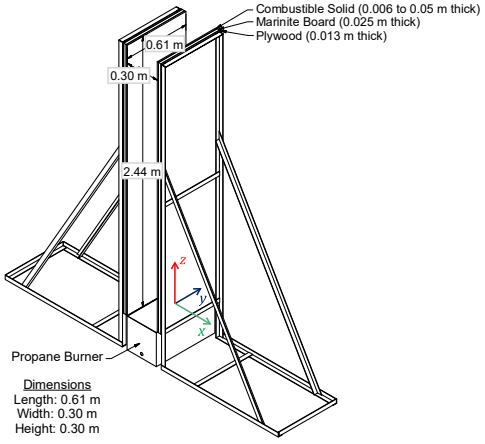

Figure 1: Schematic of the Parallel Panel Apparatus (origin of coordinate system is located at the top/center of the propane burner).

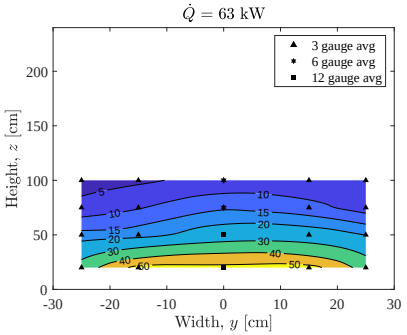

Figure 2: Spatially-resolved measurements of steady-state burner flame heat flux (final burner configuration, $\dot{Q}$ = 63 kW). The legend indicates number of gauge measurements recorded at each location.

In total, full-scale fire growth experiments were performed on 18 combustible solids including:

"Pure" Synthetic Polymers: High Density Polyethylene (HDPE), High Impact Polystyrene (HIPS), Polybutylene Terepthalate (PBT), Poly(methyl methacrylate) (PMMA), Poly(vinyl chloride) (PVC);

Copolymers: Poly(Acrylonitrile Butadiene Styrene) (ABS), PMMA-PVC alloy (Kydex);

Porous Polymer Foams: Cross Linked Polyethylene (XLPE; 3 densities), Poly(Isocyanurate) (PolyIso), Extruded Polystyrene (XPS; 2 suppliers, 3 thicknesses each);

Composite Materials: Glass-fiber-reinforced polyester resin (GPO-1 and GPO-3), Poly(oxymethylene) (POM-GF); and

Other Materials: Oriented Strand Board (OSB), Western Red Cedar (WRC), Switchboard/Panelboard wire (SIS Wire).

Spatially-resolved measurements of flame-to-surface heat transfer were made for ten of the eighteen materials tested in this study (ABS, HIPS, GPO-1, GPO-3, SIS Wire, OSB, PMMA, POM-GF, PVC, and WRC). In each test, heat flux was measured by a series of up to fourteen water-cooled Schmidt-Boelter gauges positioned flush with the front surface of the wall lining material. Gauges could be placed at nine heights (10 cm $\leq z \leq$ 220 cm) along the centerline of the panel walls. Additionally, in select tests, flame heat flux was also recorded at up to four locations across the width (y-dimension) of the panel at up to four heights (z = 0.20 m, 0.50 m, 1.0 m, and 1.8 m). In repeated tests, at least two replicate measurements were obtained at each height of interest. Details of gauge cleaning, calibration, mounting, and use as well as a complete uncertainty budget for these measurements are provided elsewhere [23]. The primary uncertainty component of measured flame heat flux is mean random error due to stochastic fluctuations; in figures below, all errors bars indicate an expanded uncertainty with coverage factor of 2 (i.e. a 95 % confidence interval).

It has been shown that representing flame heat flux as purely convective or radiative can alter numerical predictions of the flame spread rate by as much as a factor of 2 [20]. Thus, in repeated experiments on six of the materials tested here, both the total, $\dot{q}''_{\text{total}}$, and the radiative component, $\dot{q}''_{\text{rad}}$, of the flame heat flux were measured using a total heat flux gauge and a radiometer positioned side-by-side at the same height, z. These measurements were made at up to four heights, z = 0.50 m, 1.0 m, 1.8 m, and 2.2 m. To ensure accurate measurements, both gauges were covered with shields at the start of each experiment to protect them from soot and other species that could deposit at their front surfaces. The shields were removed after continuous flaming was observed across the gauge location and the fraction of heat flux attributed to radiation was calculated as $\dot{q}''_{\text{rad}}/\dot{q}''_{\text{total}}$.

3. Results

The procedure for post-processing of the flame heat flux data is as follows. First, time-resolved heat flux measurements recorded by each individual gauge (in each test) were reviewed alongside photographs, videos, and notes taken during testing to identify "good" data: i.e., when flame coverage was uniform across the sample wall and the sample itself had not deformed. Next, heat flux measurements were processed such that they could be plotted as a function of HRR, rather than time, to minimize the impact of test-to-test temporal variability. This required (1) smoothing of each data set, (2) determination of the resolution of measurements in HRR-space (i.e., 'given instantaneously-measured fire growth rates for each material and a data reporting frequency of Δt=1 s, what is the finest interval, $\Delta\dot{Q}$ [kW], at which measurements were reported?'), and (3) interpolation of measurements onto uniformly-spaced intervals of HRR such that statistics could be calculated for repeated heat flux measurements. Finally, average profiles — e.g., evolution of flame heat flux at a given location with increases in HRR or spatially-resolved flame heat feedback profiles across the surface of the panels at a given HRR — were calculated and presented using this processed data.

Figure 3 plots spatially-resolved heat flux profiles along with representative images of flame structure during flame spread over PMMA at heat release rates between 120 kW $\leq \dot{Q} \leq$ 2800 kW. As flames first begin to spread, elevated heat fluxes are recorded at progressively higher heights, z. When the HRR is approximately 500 kW, flames are observed at the top of the panel walls and measured heat flux exceeds 50 kW/m^2 across the height of samples. As the HRR continues to increase, flames thicken, and measured heat flux increases at all heights.

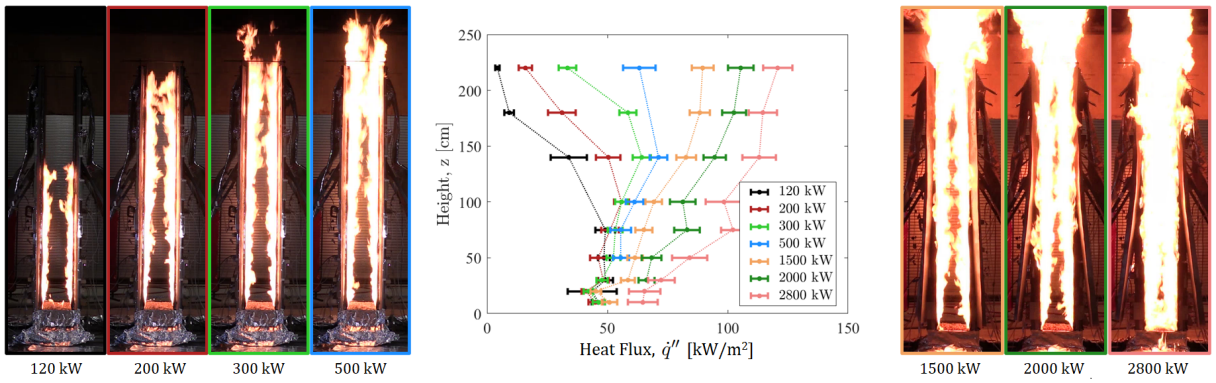

Figure 3: PMMA flame structure and vertical profiles of heat flux at 120 kW $\leq \dot{Q} \leq$ 2800 kW.

Figure 4 plots heat flux profiles measured for multiple materials at three heat release rates: 200 kW, 800 kW, and 3 MW. Differences in peak heat flux can be observed at nominally the same fire size for different fuels, potentially due to sooting propensity. Note that in Fig. 4a, the elevated heat fluxes measured at heights $z \leq 0.75$ m during tests on OSB and Western Red Cedar likely arise due to the presence of flames supported by the propane burner (which was left on to ensure the continued burning of these two materials but turned off during tests on each of the other materials shown in this figure) and smoldering of the wood panels near the burner.

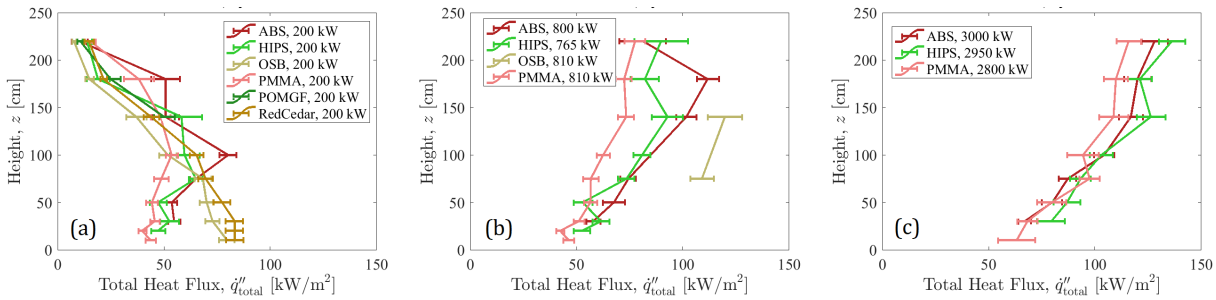

Figure 4: Height-resolved measurements of total wall flame heat flux measured at the centerline, $y = 0$, of panels during repeated experiments (on ABS, HIPS, OSB, PMMA, POM-GF, and WRC) at (a) $\dot{Q} = 200$ kW, (b), $\dot{Q} = 800$ kW and (c) $\dot{Q} = 3000$ kW.

Figure 5 plots time-resolved measurements of $\dot{q}''_{rad}$ and $\dot{q}''_{total}$ recorded by two pairs of shielded heat flux gauges positioned at $z = 1.0$ m and $z = 1.8$ m (from a representative test on OSB). A rapid increase in measured heat flux was observed when the gauge shields were removed at $t = 180$ s (similar rapid increases were observed in all tests, whenever the shields were removed successfully). Although continuous flaming was observed across the surface of each heat flux gauge when shields were removed, in most cases measured flame heat flux, especially $\dot{q}''_{rad}$, decreased after shield removal. $\dot{q}''_{rad}$ and $\dot{q}''_{total}$ are therefore reported as discrete values: i.e., the maximum average heat flux (6 s running average) recorded within 10 s of shield removal.

This subset of measurement data used is highlighted by the solid black symbols plotted in Fig. 5. Calculated values of the radiative fraction of wall flame heat flux, $\dot{q}''_{\text{rad}}/\dot{q}''_{\text{total}}$, are plotted in Fig. 6; as seen here, $\dot{q}''_{\text{rad}}/\dot{q}''_{\text{total}}$ varies with material composition and may correlate with material sooting propensity. For the least sooty of these fuels, POM-GF, which produced a blue, nearly transparent flame, the radiative fraction averaged just 0.16. Conversely, for ABS and HIPS, which supported large, sooty fires, the radiative fraction is closer to 0.40. Note that this average does not include the two highest radiative fractions measured in ABS Test R2, approximately 0.58 and 0.70, which were both obtained shortly after peak HRR was observed when ABS samples had completely detached from the apparatus walls due to softening/burnout at attachment points but continued to burn at the base of the assembly.

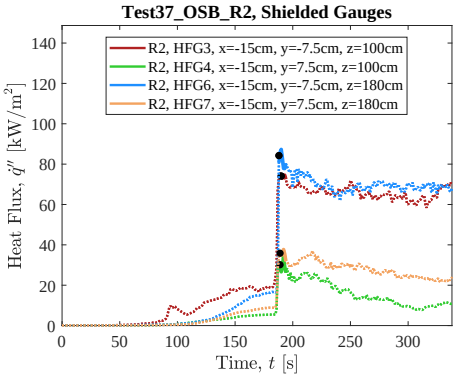

Figure 5: Measured total and radiation heat flux at $z = 1.0$ m and $z = 1.8$ m during a representative test on OSB.

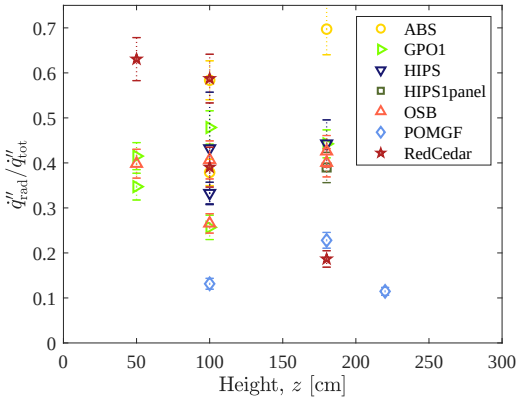

Figure 6: Measured radiative fraction of wall flame heat flux, $\dot{q}''_{\text{rad}}/\dot{q}''_{\text{total}}$, when continuous flaming was supported across the panel walls.

4. Conclusions

This paper presents a subset of measurements obtained from a series of 90 full-scale fire experiments, including 66 conducted on 18 unique combustible solids. The primary focus of this research is to quantify how material composition (materials of varied chemical composition that support different burning behaviors such as swelling, charring, dripping, and soot formation) affects ignition, flame heat flux and structure, fire growth, and peak fire size in large fires. Here, special emphasis is placed on spatially-resolved flame heat flux profiles that can be used as a validation set for CFD models.

Acknowledgments

This work was supported by the Office of Nuclear Regulatory Research of the US Nuclear Regulatory Commission (US NRC); this program was directed by Mark Henry Salley. The large scale experiments described in this report were conducted at the National Fire Research Laboratory (NFRL) at NIST, which is directed by Matt Bundy. Technical support for the experiments was provided by NFRL staff members; their efforts and expertise made these experiments possible.

References

[1] Bruns, M.C., Leventon, I.T., Design of a Material Flammability Property Database," American Chemical Society National Meeting, 2016.

[2] Leventon, I.T., Heck, M.V., Bruns, M.C., McGrattan, K.B., Davis, R.D., "Experimental Measurement of Material Flammability at the Micro-, Bench-, and Full-Scales for Fire Model Development" ASTM Symposium on Obtaining Data for Fire Models, 2021.
[3] Bruns, M.C., Leventon, I.T., "Automated fitting of thermog ravimetric analysis data," Fire & Materials, 2021.
[4] Bruns, M.C., Leventon, I.T., "Automated Characterization of Heat Capacities and Heats of Gasification of Combustion of Flammable Materials," FAA Fire & Cabin Safety Research Conference, 2022.
[5] Bruns, M.C., Leventon, I.T., "Development of Automated Calibration Tools for Determining Fire Model Input Parameters," American Chemical Society - Fire and Polymers, 2022.
[6] McGrattan, K., Hostikka, S., Floyd, J., McDermott, R., Vanella, M., Mueller, E., "Fire Dynamics Simulator Technical Refernce Guide Volume 3: Validation. NIST Special Publication 1018-3.
[7] Nyazika, T., Jimenez, M., Samyn, F. and Bourbigot, S., "Pyrolysis modeling, sensitivity analysis, and optimization techniques for combustible materials: A review," Journal of Fire Sciences, 2019.
[8] Batiot, B., Bruns, M., Hostikka, S., Leventon I.T., Nakamura, Y., Reszka, P., Rogaume, T., Stoliarov, S.I., "Preliminary Summary of Experimental Results Submitted to the 2021 MaCFP Condensed Phase Workshop," MaCFP Predecisional Report, 2020.
[9] Ding, Y., Fukumoto, K., Ezekoye, O.A., Lu, S., Wang, C. and Li, C., "Experimental and numerical simulation of multi-component combustion of typical charring material," Combustion and Flame, 2020.
[10] Stoliarov, S.I. and Li, J., "Parameterization and validation of pyrolysis models for polymeric materials," Fire Technology, 2016.
[11] Hehnen, T., Arnold, L., "PMMA pyrolysis simulation–from micro-to real-scale," Fire Safety Journal, 2023.
[12] Rinta-Paavola, A. and Hostikka, S., "A model for the pyrolysis of two Nordic structural timbers," Fire and materials, 2022.
[13] Girardin, B., Fontaine, G., Duquesne, S., Försth, M. and Bourbigot, S., "Measurement of kinetics and thermodynamics of the thermal degradation for flame retarded materials: application to EVA/ATH/NC," Journal of Analytical and Applied Pyrolysis, 2017.
[14] Chaos, M., Khan, M.M., Krishnamoorthy, N., de Ris, J.L. and Dorofeev, S.B., "Evaluation of optimization schemes and determination of solid fuel properties for CFD fire models using bench-scale pyrolysis tests." Proceedings of the Combustion Institute, 2011.
[15] Federal Aviation Administration Fire Safety, "Cone Calorimeter Data ASTM E1354", Accessed: https://www.fire.tc.faa.gov/ConeCalorimeterDataMining/calorimeter.asp
[16] The Measurement and Computation of Fire Phenomena (MaCFP) Repository. Accessed: https://github.com/MaCFP/
[17] McKinnon M, Weinschenk C., Madrzykowski, D., "Materials and Products Database Technical Reference Guide," Technical report, Fire Safety Research Institute, UL Research Institutes, 2023.
[18] Kacem, A., Mense, M., Pizzo, Y., Boyer, G., Suard, S., Boulet, P., Parent, G. and Porterie, B., "A fully coupled fluid/solid model for open air combustion of horizontally-oriented PMMA samples," Combustion and Flame, 2016.
[19] Leventon, I.T., Li, J. and Stoliarov, S.I., "A flame spread simulation based on a comprehensive solid pyrolysis model coupled with a detailed empirical flame structure representation," Combustion and Flame, 2015.
[20] Chaudhari, D.M., Fiola, G.J. and Stoliarov, S.I., "Experimental analysis and modeling of Buoyancy-driven flame spread on cast poly (methyl methacrylate) in corner configuration," Polymer Degradation and Stability, 2021.
[21] Fukumoto, K., Wang, C. and Wen, J., "Large eddy simulation of upward flame spread on PMMA walls with a fully coupled fluid–solid approach," Combustion and Flame, 2018.
[22] Zeinali, D., Gupta, A., Maragkos, G., Agarwal, G., Beji, T., Chaos, M., Wang, Y., Degroote, J. and Merci, B., 2019. Study of the importance of non-uniform mass density in numerical simulations of fire spread over MDF panels in a corner configuration. Combustion and Flame, 200, pp.303-315.
[23] Leventon, I.T., Heck, M.V, McGrattan, K.B, Bundy, M.F. and Davis, R.D., "The Impact of Material Composition on Ignitability and Fire Growth. Volume 1: Full-Scale Burning Behavior of Combustible Solids Commonly Found in Nuclear Power Plants," Technical Note (NIST TN2282), 2024.
[24] Tewarson,A. Khan, M., Wu, P.K., and Bill, R.G., "Flammability evaluation of clean room polymeric materials for the semiconductor industry," Fire and Materials, 2001.
[25] FM Approvals LLC. American National Standard for Cleanroom Materials Flammability Test Protocol. Standard ANSI/FM 4910-2021, Norwood, MA, USA, 2021.

Full-Scale Burning Behavior of Combustible Solids—The Impact of Material Composition on Fire Growth, Flame Structure and Heat Feedback
Supplemental Information

Isaac T. Leventon, Michael V. Heck, Kevin B. McGrattan, Matthew F. Bundy, Rick D. Davis*

100 Bureau Drive; Gaithersburg, MD 20878; United States of America

As illustrated in Fig. 7 (measurements from tests conducted on PMMA), time-resolved measurements of heat flux (Fig. 7a) and HRR (Fig. 7b) obtained in each test replicate are analyzed together to determine spatially resolved heat flux profiles at different fire sizes. First, clean heat flux measurements recorded at the same location in different tests are identified; this data is then smoothed, averaged together by analyzing them as a function of fire size (i.e., HRR; (Fig. 7c)), and interpolated onto uniformly-spaced intervals of HRR such that statistics could be calculated for repeated heat flux measurements. This process is repeated at all measurement locations (Fig. 7d) and spatially-resolved heat feedback profiles are determined based on these average curves (Fig. 7e). Vertical lines in Fig. 7d highlight the average heat flux values used to define spatially-resolved profiles plotted in Fig. 7e.

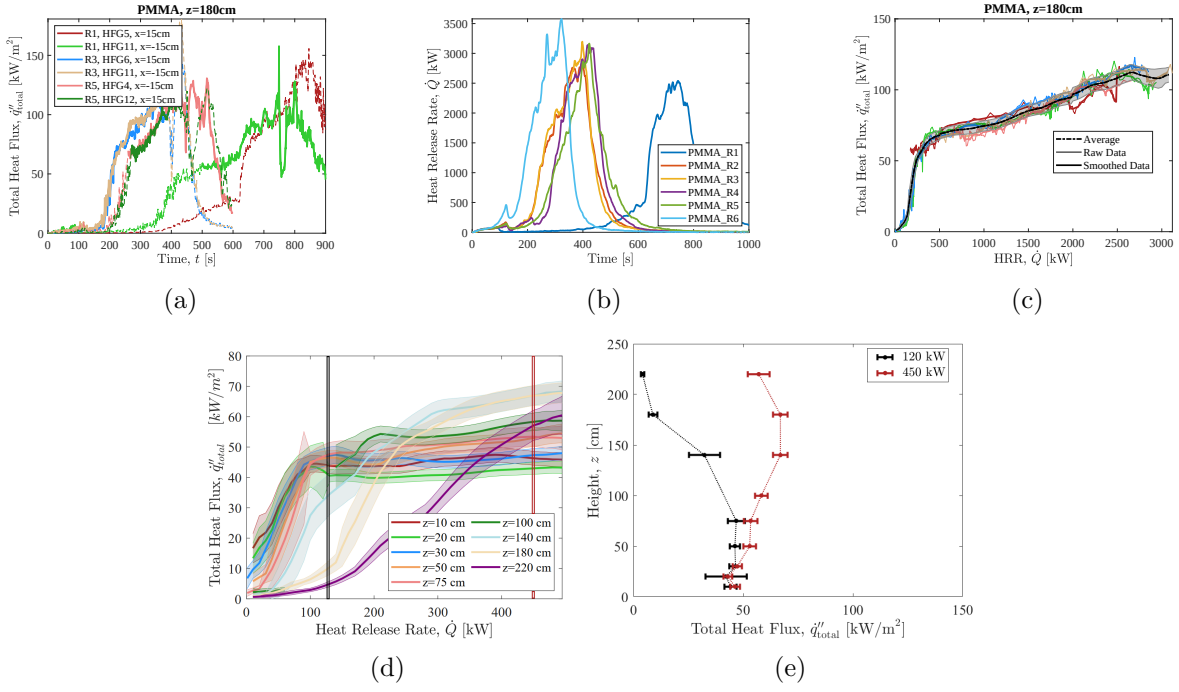

Figure 7: Analysis of total heat flux ($\dot{q}''$) and HRR data to provide spatially-resolved wall flame heat flux profiles during tests on poly(methyl methacrylate), PMMA. (a) Time-resolved measurements of heat flux recorded at $z = 180$ cm; (b) Time-resolved HRR measured in six repeated tests; (c) Heat flux versus HRR at $z = 180$ cm; (d) Average heat flux curves at all heights, z, versus HRR; (e) Spatially resolved heat flux profiles at 120 kW and 450 kW.